Upper-mantle anisotropy in the southeastern margin of the Tibetan Plateau revealed by fullwave SKS splitting intensity tomography

Yi Lin[1,2], Li Zhao[1,3]

[1] School of Earth and Space Sciences, Peking University, Beijing 100871, China.

[2] Key Laboratory of Earth Exploration and Information Techniques of the China Ministry of Education, Chengdu University of Technology, Chengdu 610059, China.

[3] Hebei Hongshan National Geophysical Observatory, Peking University, Beijing 100871, China.

Corresponding author: L. Zhao (lizhaopku@pku.edu.cn)

Key Points:

- A 3D shear-wave anisotropy model for the SE margin of the Tibetan Plateau is obtained by fullwave SKS splitting intensity tomography
- Anisotropy distribution shows a decoupling of the deformations in the lithosphere and asthenosphere
- Lithospheric anisotropy has a complex pattern, whereas asthenospheric anisotropy follows the APM

Abstract

The southeastern margin of the Tibetan Plateau has experienced complex deformation since the Cenozoic, resulting in a high level of seismicity and seismic hazard. Knowledge about the seismic anisotropy provides important insight into the deformation mechanism and the regional seismotectonics beneath this tectonically active region. In this study, we conduct a fullwave multi-scale tomography to investigate the seismic anisotropy in the southeastern margin of the Tibetan Plateau. Broadband records from 470 teleseismic events at 111 permanent stations in the region are used to obtain 5,216 high-quality SKS splitting intensity measurements, which are then inverted in conjunction with 3D sensitivity kernels to obtain the anisotropic model for the region with a multi-scale resolution. Resolution tests show that our dataset recovers anisotropy anomalies reasonably well on the scale of 1º x 1º horizontally and ~100 km vertically. Our result suggests that in the southeastern margin of the Tibetan Plateau the deformations in the lithosphere and asthenosphere are decoupled. The anisotropy in the lithosphere varies both laterally and vertically as a result of the dynamic interactions of neighboring blocks as well as lithospheric reactivation. The anisotropy in the asthenosphere largely follows the direction of regional absolute plate motion, i.e. southeastward under the Songpan-Ganzi Terrane and the Yangtze Craton and nearly east-west south of 26ºN latitude. The SKS splitting observed at the surface can be interpreted as the vertical integration of the contributions from lithosphere and asthenosphere.

Keywords: seismic anisotropy; splitting intensity; finite-frequency; fullwave tomography; southeastern Tibetan Plateau

Plain Language Summary

The southeastern margin of the Tibetan Plateau has experienced significant deformation since the

Cenozoic due to the collision with the Indian Plate in the south and interactions with the Yangtze Craton in the east. Knowledge about the upper mantle seismic anisotropy helps us understand the reginoal deformation and dynamic evolution. In this study, we conduct a fullwave multi-scale anisotropy tomography for the southeastern margin of the Tibetan Plateau using 5,216 high-quality SKS splitting intensity measurements obtained from the broadband records of 470 teleseismic events at 111 stations. Our result shows a decoupling between the lithosphere and asthenosphere deformations in the southeastern margin of the Tibetan Plateau. The anisotropy in the lithosphere varies both laterally and vertically as a result of the dynamic interactions of neighboring blocks as well as lithospheric reactivation. The anisotropy in the asthenosphere is largely parallel to the regional absolute plate motion, and the SKS splitting observed at the surface is the result of vertical integration of the contributions from lithosphere and asthenosphere.

1 Introduction

The ongoing Indian-Eurasian continental collision since 50 Ma has resulted in the greatest plateau on Earth and deformed large parts of central and east Asia (Yin & Harrison, 2000; Kind et al., 2002). Despite decades of study, questions remain over the dynamics of the lithospheric deformation and asthenosphere flow beneath the Tibetan Plateau and the surrounding regions (Royden et al., 2008).

The region in the southeastern margin of the Tibetan Plateau involves many active tectonic blocks (Figure 1), including the Songpan-Ganzi Terrane (SGT), the Sichuan Basin (SCB), the Sichuan-Yunnan Rhombic Block (SYRB), the Indo-China Block (ICB), the Qiangtang Block (QTB), and the Yangtze Craton (YTC). The SGT is part of central Tibetan Plateau. Its eastern part is separated from the SCB and SYRB by the Longmenshan Fault (LMSF) and Lijiang-Xiaojinhe Fault (LJ-XJHF), respectively, and bounded in the south by the Jinshajiang Fault (JSJF) from the QTB. The convergence between the Indian and Eurasian plates caused the SGT to expand eastward against the SCB during the Cenozoic (Yin & Harrison, 2000). GPS observations show eastward crustal motion of the eastern SGT with the crustal strain rate decreasing abruptly from ~20 mm/year (relative to the YTC reference frame) in the interior SGT to ~3–4 mm/year or less in the vicinity of central and southern segments of the LMSF, indicating that the eastward expansion of the SGT is apparently resisted by the SCB (Shen et al., 2005; Zhang, 2013). Low-velocity zones and high-conductivity bodies in the mid-lower crust under the SGT revealed by geophysical studies (Zhao et al., 2012; Bao et al., 2020) suggest the existence of mid-lower crustal flow. However, these geophysical anomalies exhibit strong lateral heterogeneity in eastern Tibet, implying a complex internal deformation process. The SCB and SYRB are both parts of the YTC (Zhang et al., 2013; Li et al., 2021). The former forms the rigid and stable northwestern margin of the YTC, while the crust of the latter is extruding southeastward along the Anninghe-Zemuhe Fault (ANH-ZMHF) and Xiaojiang Fault (XJF) in the east and the Red River Fault (RRF) in the southwest (Zhang et al., 2003). The Lancangjiang Fault (LCJF) separates the narrow QTB in the east and the ICB in the west. Crustal movements are predominantly characterized by a clockwise rotation around the Eastern Himalayan Syntaxis (EHS), transforming the movement of the plateau material from eastward north of the syntaxis to southeastward and southward further south (Wang & Shen, 2020).

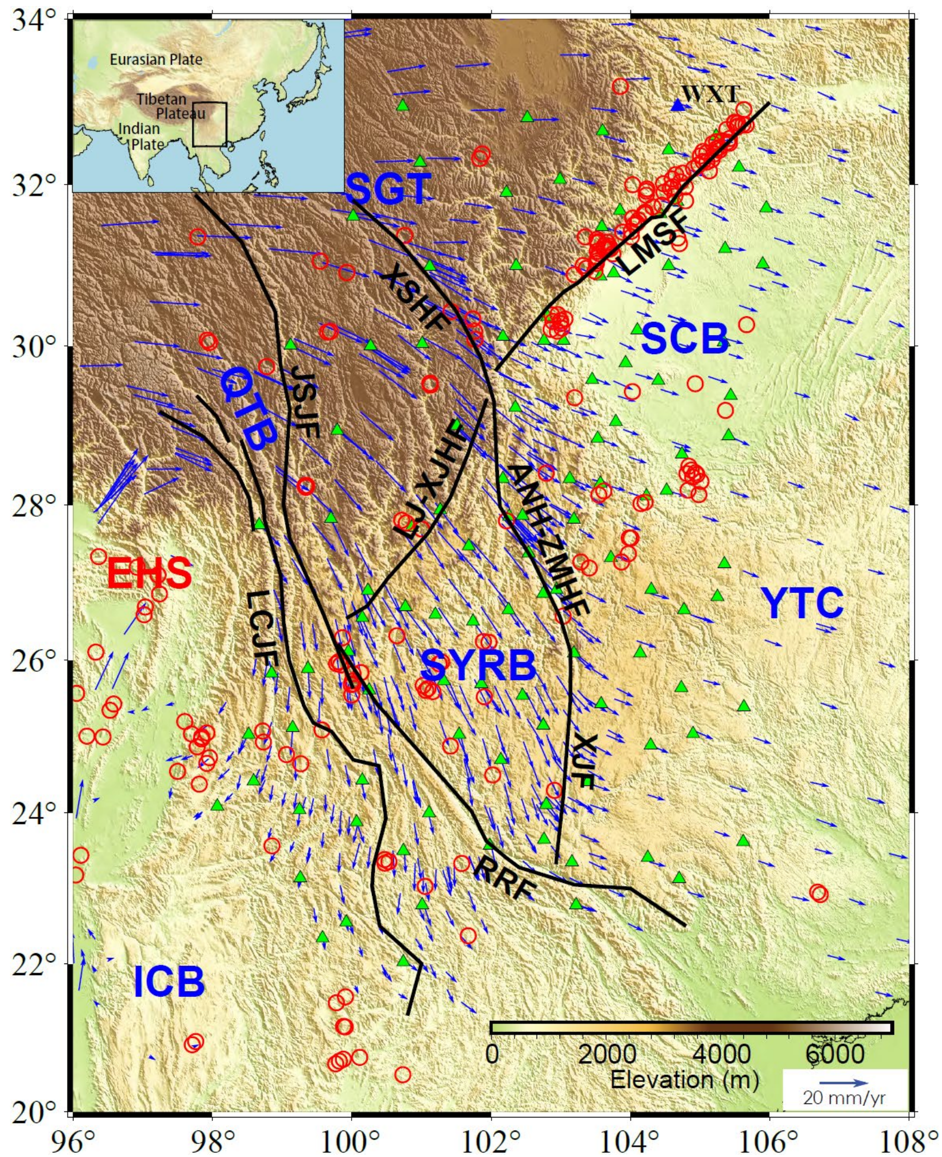

Figure 1. Map of the tectonic environment of southeastern margin of the Tibetan Plateau with seismic stations (green-filled triangles) and epicenters (red open circles) of earthquakes of

magnitude 5 and above from 2000 to 2022. The blue triangle marks the station WXT for which SKS waveforms, splitting intensities and sensitivity kernels are shown in Figures 4, 5 and 7, respectively. Major active faults are shown by thick black lines with abbreviated names in black, including LMSF: Longmenshan Fault; XSHF: Xianshuihe Fault; JSJF: Jinshajiang Fault; LCJF: Lancangjiang Fault; LJ-XJHF: Lijiang-Xiaojinhe Fault; ANH-ZMHF: Anninghe-Zemuhe Fault; XJF: Xiaojiang Fault; and RRF: Red River Fault. Major active tectonic blocks are indicated by abbreviated texts in blue, including SGT: Songpan-Ganzi Terrane; SCB: Sichuan Basin; QTB: Qiangtang Block; SYRB: Sichuan-Yunnan Rhombic Block; YTC: Yangtze Craton; and ICB: Indo-China Block. EHS stands for the Eastern Himalaya Syntax. Blue arrows show the GPS velocities with respect to the Eurasian Plate (Wang & Shen, 2020). Background color shows the topography. The black box in the inset map indicates the location of the main figure.

Over the past two decades, and in particular after the 12 May 2008 Wenchuan Mw7.9 earthquake on the LMSF, a large number of seismic stations have been deployed in the southeastern margin of the Tibetan Plateau. Waveforms recorded by the growing number of broadband stations have provided crucial data for studying the structure and dynamics of the crust and upper mantle beneath the region, such as the variation in crustal thickness (Wang et al., 2017; Xu et al., 2020), the widespread low-velocity anomalies in mid-lower crust revealed by receiver function analysis (Hu et al., 2005; Xu et al., 2007; Zhang et al., 2009; Wang et al., 2010), Lg-wave high-attenuation zones (Zhao et al., 2013; Wei & Zhao, 2019), joint inversion of receiver function and surface wave dispersion (Liu et al., 2014), and body- and surface-wave tomographies (Huang et al., 2002; Wang et al., 2003; Huang et al., 2009; Li et al., 2009; Wei & Zhao, 2022; Yang et al., 2019).

Across the LMSF, the drastic change in elevation from ~5–6 km in the west to a few hundred meters in the east suggests large variation in the lithospheric thickness. Figure 2 shows the LITHO1.0 model (Pasyanos et al., 2014) in the study region, where the lithosphere has a thickness of less than 100 km in the northern and southern parts but ~150 km in mid latitudes. The thickest lithosphere in the study region is more than 200 km beneath the SCB.

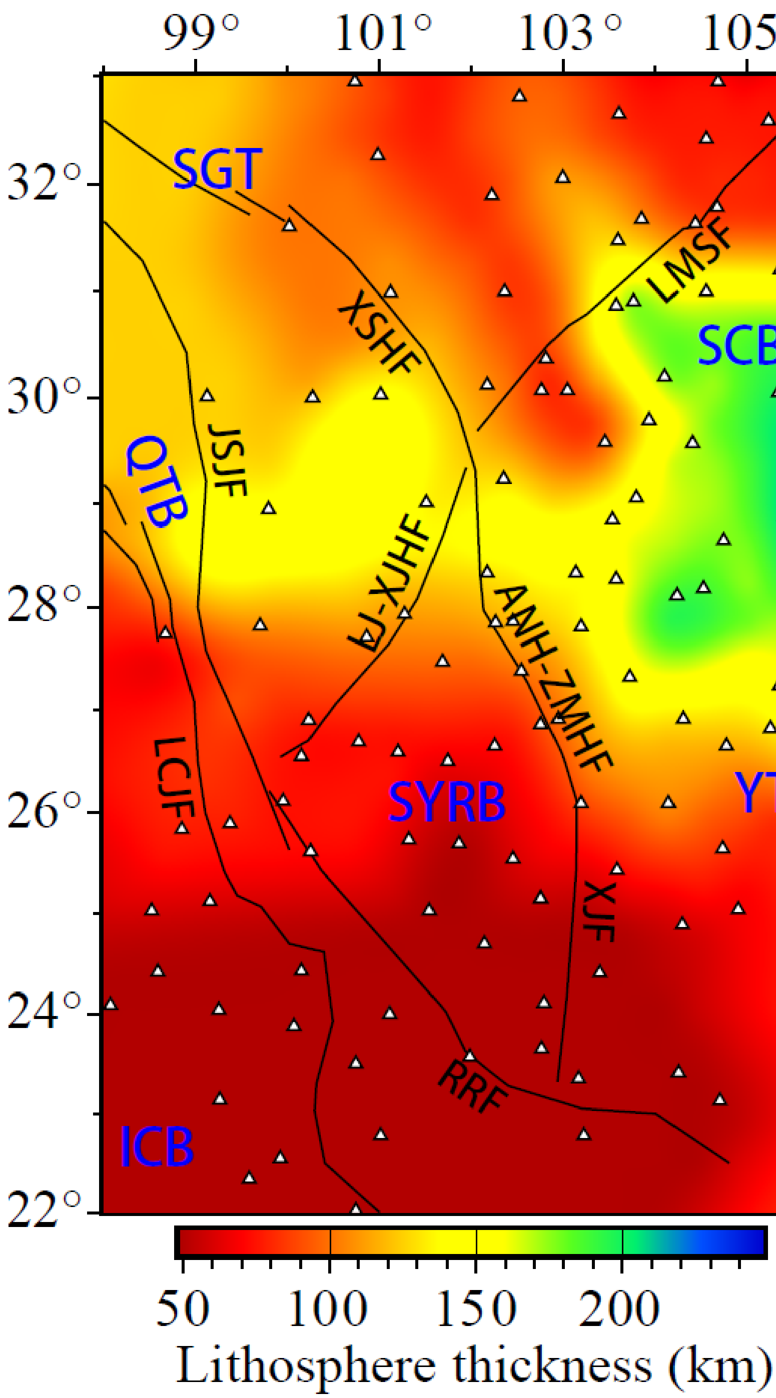

Figure 2. Lithosphere thickness in model LITHO1.0 (Pasyanos et al., 2014). Names of major faults and tectonic blocks are the same as in Figure 1.

Distribution of azimuthal anisotropy is an important proxy for deformation. There have been numerous studies devoted to the crustal anisotropy beneath the southeastern Tibetan Plateau utilizing different methods, such as the Pms splitting (Sun et al., 2012; Cai et al., 2016; Han et al., 2020), anisotropic tomography of P and Pn waves (Lei et al., 2014; Huang et al., 2018), surface wave anisotropic tomography (Yang et al., 2010; Yao et al., 2010; Legendre et al., 2015; Zhang et al., 2023), and the splitting of shear waves (Shi et al., 2012). In the upper crust, the fast axis directions are mainly parallel to the strike of active faults (e.g., Yao et al., 2010; Shi et al., 2012; Huang et al., 2018), whereas the anisotropic pattern in the lower crust is different. Huang et al. (2018) showed that the fast velocity direction deviates from the strikes of active faults significantly using P-wave anisotropic tomography. Han et al. (2020) used the Markov-chain Monte Carlo inversion of receiver functions to isolate the effect of potential dipping interfaces. Their results showed that the fast axis directions in the lower crust are in good agreement with the topography contours, implying that the gravitational potential may be the driving force for the crustal deformation in southeastern Tibet.

The XKS-wave splitting is routinely used to probe the anisotropic structure in the upper mantle (Long & Becker, 2010). Flesch et al. (2005) conducted joint analysis of GPS, surface geology and shear-wave splitting measurements to argue for a vertically coherent deformation in the crust and upper mantle in the Tibetan Plateau but a decoupling beneath Yunnan Province in southwestern China. Lev et al. (2006) also supported the decoupling beneath Yunnan using shear-wave splitting observations, but they were not able to constrain the level of coupling beneath the Tibetan Plateau. Based on a joint analysis using more shear-wave splitting measurements and GPS observations, Wang et al. (2008) argued for the crust-mantle coupling in the Tibetan Plateau and the surrounding regions.

Substantial efforts have been made to develop a theoretical framework as well as practical strategies for the inversion of 3D distribution of anisotropy. A fullwave approach has been developed for the measurement of shear-wave splitting intensities and interpretation in terms of shear-wave azimuthal anisotropy parameters (Chevrot, 2000; Favier & Chevrot, 2003; Chevrot, 2006; Sieminski et al., 2008; Monteiller & Chevrot, 2011; Lin et al., 2014a), which has been applied to anisotropy tomographies for southern California (Monteiller & Chevrot, 2011; Lin et al., 2014b), the High Lava Plain (Mondal & Long, 2020), and the southeastern Tibetan Plateau (Huang & Chevrot, 2021). The depth variations of anisotropy obtained by these studies have shed new lights in understanding the sources of anisotropy and the associated mantle dynamics.

In this study, we conduct a fullwave multiscale anisotropy tomography for the southeastern margin of the Tibet Plateau. We collect seismic records at regional permanent broadband stations from globally distributed earthquakes and obtain high-quality measurements of SKS splitting intensities. We then invert the splitting intensities using a wavelet-based parameterization of the 3D model to achieve a multi-scale resolution to the anisotropic structure. We also provide an interpretation of our anisotropic model for the southeastern margin of the Tibet Plateau in terms of regional geodynamics.

2 Data and Methods

2.1 Waveform records

We collect waveforms recorded by 111 permanent broadband stations (green triangles in Figure 1) deployed in the study region. To guarantee a wide range of azimuthal distribution, we select events of magnitude Mw $\geq$ 5.5 from 2009 to 2020, located in the epicentral distance range of 90°–130°. After quality control of the waveforms and removal of outliers of the data (see Section 2.2), a total of 470 events are used in the subsequent inversions. Figure 3 displays the event distribution.

2.2 Splitting intensity measurements

Shear wave splitting measurement is nowadays a routine procedure in the study of seismic anisotropy. Several previous studies have documented the measured SKS splitting parameters (fast directions and delay times) at stations in our study region (e.g., Chang et al., 2015; Yang et al., 2018; Liu et al., 2020; Huang & Chevrot, 2021; Li et al., 2021). In this study, we invert for the 3D anisotropy structure using the splitting intensity (SI) measurements obtained by computing the zero-lag cross-correlation between the transverse-component record and the time derivative of the radial-component record (Chevrot, 2000).

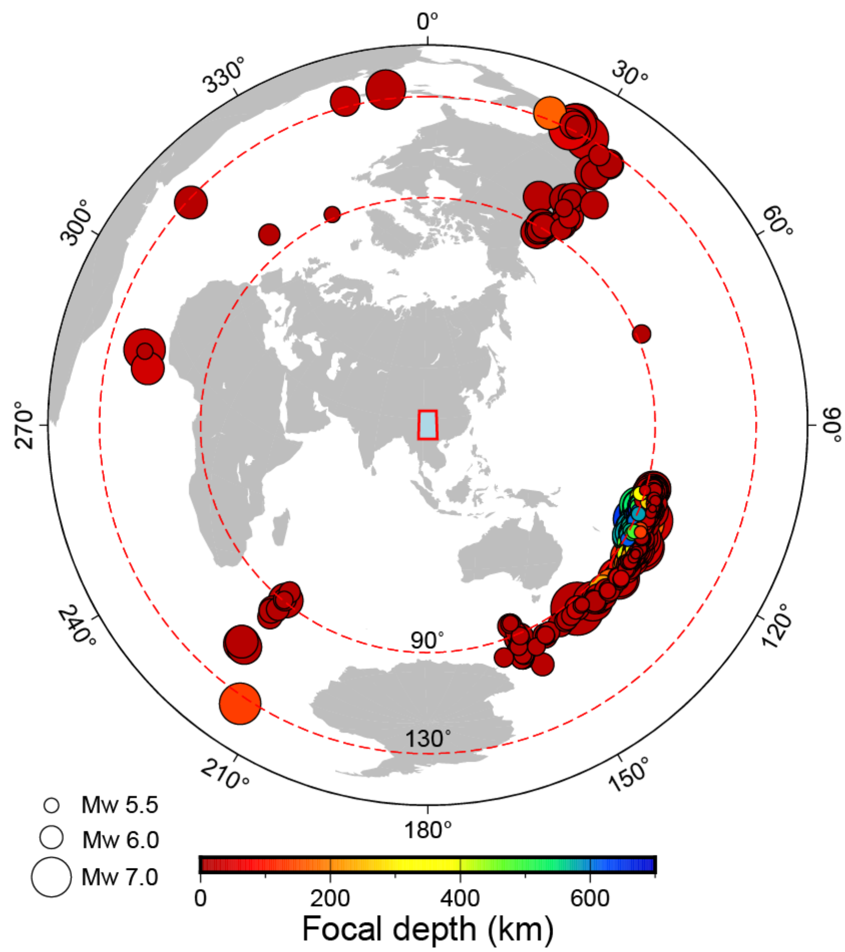

Figure 3. Distribution of 470 teleseismic events used for SKS splitting intensity inversion in this study. Events of magnitudes Mw5.5 and greater in the epicentral distance range of 90°–130° during 2009–2020 are selected. The red box in the center indicates the study area.

For a given station, the SI of the SKS wave from the *i*-th event is defined as

$$S_i = -2\frac{\int_{t_{i1}}^{t_{i2}} \dot{u}_i^R(t)u_i^T(t)dt}{\int_{t_{i1}}^{t_{i2}} [\dot{u}_i^R(t)]^2dt}, \tag{1}$$

where $[t_{i1}, t_{i2}]$ is the time window for the SKS wave, and $u_i^R(t)$ and $u_i^T(t)$ are the radial and transverse-component records, respectively, from the i-th event. A dot above a variable indicates derivative with respect to time. The conventional SKS splitting parameters at the given station, namely the fast-direction azimuth θ and delay time Δt, are related to the SIs measured at the station from all events through a sinusoidal curve fitting (Chevrot, 2000; Lin et al., 2014a):

$$S_i = \Delta t \sin 2(\theta - \theta_i^b), \tag{2}$$

where θ_i^b is the back azimuth of the i-th event.

In this study, we obtain the SI measurements of SKS waves with the help of SplitRacer (Link et al., 2022), an efficient and automatic toolbox developed for the measurement and quality control of XKS splittings. An example of the SplitRacer processing is shown in Figure 4. We use SplitRacer to determine the SKS time window automatically, followed by a manual check on the quality of the SKS signals. Then, we calculate the SIs using Eq. (1). The period band we use in this study is 8–50 s considering the dominant periods of the SKS signals as well as minimizing the interference with neighboring phases. As shown in Figure 4, the spectral powers of the radial- and transverse-component records are calculated by the short-time Fourier transform (Quatieri, 2006) and summed. Then, the dominant frequency band of the SKS waveform can be identified (between the red dashed horizontal lines in Figure 4c). At each time, the powers within the dominant frequency band are summed (Figure 4d), which defines the SKS window by the two crossing points at 50% of the peak level (vertical green lines in Figure 4d). The final SKS window is given by either expanding or shrinking the 50% energy window to a fixed 30-s window (red vertical lines). After completing the quality check using SplitRacer, we obtain a total of 12,457 SKS wave SI measurements.

Following Chevrot (2000), we estimate the uncertainty of each SI measurement using the following equation

$$\sigma_i = \sqrt{\frac{1}{N_i}\left\{\sum_{j=1}^{N_i}\left[u_i^T(t_j)\right]^2 - \frac{S_i^2}{4}\sum_{j=1}^{N_i}\left[\dot{u}_i^R(t_j)\right]^2\right\}}, \quad (3)$$

where S_i is the i-th SI measurement, and N_i is the number of time samples used for the window to obtain the measurement.

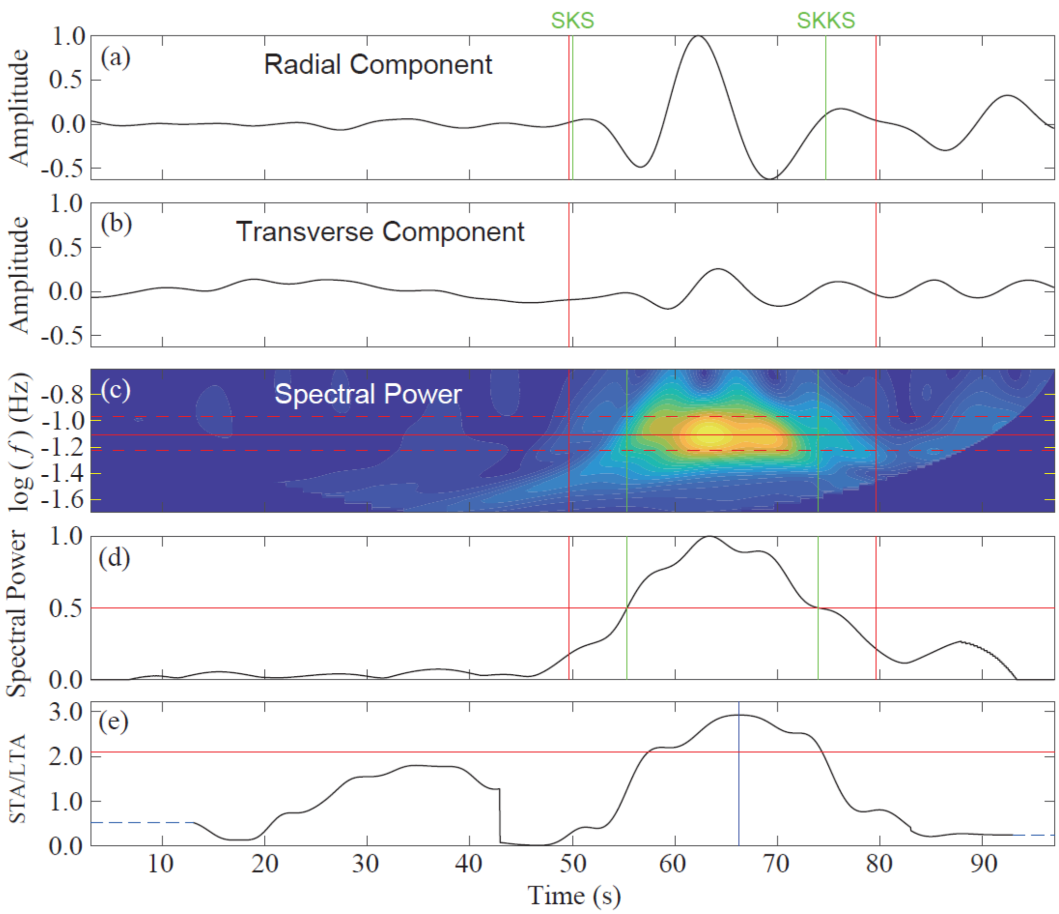

Figure 4. Example of SKS window selection using SplitRacer. (a) and (b) show normalized radial and transverse records, respectively, around the SKS arrival at station WXT (blue triangle in Figure 1) from the 24 June 2019 earthquake in New Zealand with a back azimuth of 122º. The green lines mark the theoretical SKS and SKKS arrival times of seismic phases corresponding to the event of interest. Red vertical lines mark the start and end time of the final window containing the SKS waveform. (c) Summed spectral power of the spectrogram of the radial and transverse records in (a) and (b). The red horizontal line marks the frequency of maximum spectral power, and the red dashed lines show the frequency bounds of more than 80% of the maximum. The green vertical lines mark the time window in which the summed spectral power is more than 50% of the

maximum. (d) Summed spectral power over all frequencies. The green vertical lines mark the time window in which the summed spectral energy is more than 50% of the maximum. (e) STA/LTA ratio of the radial-component record used as quality check. The blue vertical line denotes the time when the STA/LTA ratio reaches its peak within the window determined in (d). The red horizontal line is the acceptance threshold of 2.1 (Link et al., 2022).

We further clean our dataset of outliers based on two criteria: (1) At a given station, SI measurements with uncertainties σ_i larger than 1.5 times the average uncertainty $\bar{\sigma}$ for that station, i.e. $\sigma_i > 1.5\bar{\sigma}$, are removed; (2) all SI measurements at a given station are fit by a sinusoidal curve, and measurements that deviate from the sinusoidal curves by more than $2\sigma_i$ are also removed. After removing the outliers, we retain a total of 5,216 high-quality SI measurements as our final dataset for subsequent anisotropy inversion. The standard deviation of the final dataset (the average of uncertainties of all retained data) is 0.074 s. Figure 5 shows the effect on the distribution of SI measurements before and after applying the above two criteria for station WXT, which reduces the number of SI data from 184 to 61.

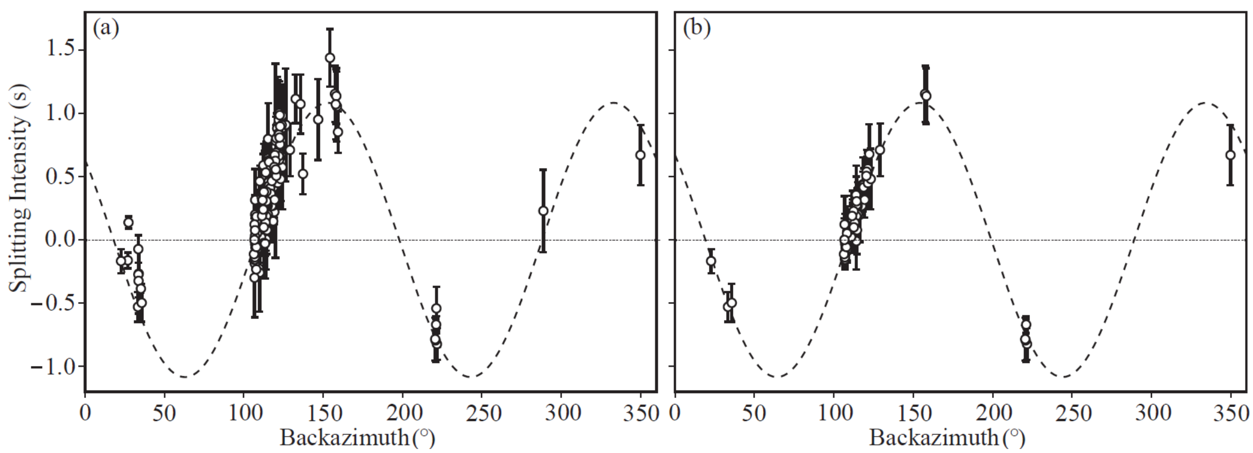

Figure 5. Variations of measured SI with event back azimuth for station WXT (blue triangle in Figure 1) before (a) and after (b) removal of SI outliers. The vertical error bars show two standard deviations ($2\sigma_i$) of individual measurements. The dashed lines represent the sinusoidal curves that best fit the measurements. According to Eq. (2), the conventional SKS splitting parameters for this station are: $\Delta t = 1.08$ s and $\theta = 109.14°$.

Based on Eq. (2), we can obtain the conventional fast-direction azimuth θ and delay time Δt at each station using all the SI measurements, and they are displayed in Figure 6. The spatial distribution of θ has a similar pattern as seen in previous studies, i.e. a generally NW-SE oriented fast axis and a nearly uniform EW alignment of the fast-axis directions south of ~26ºN latitude.

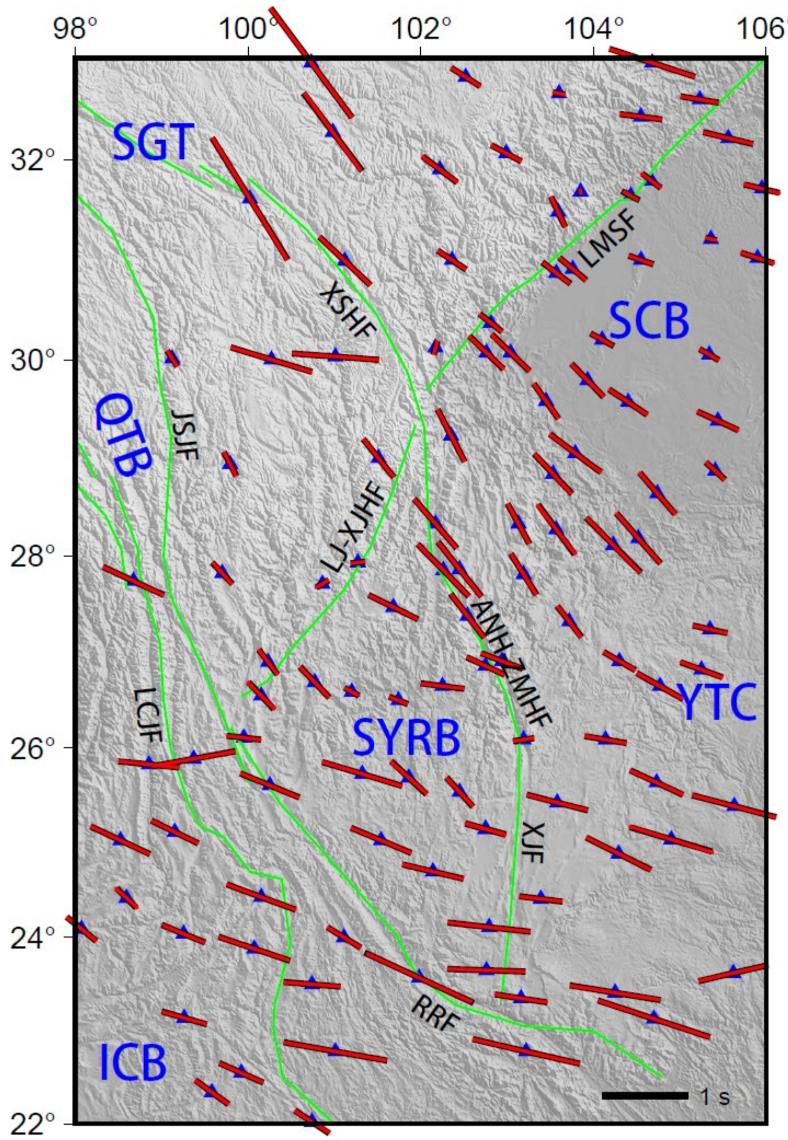

Figure 6. Black line segments show the conventional SKS fast-direction azimuths and delay times at all station obtained from the SI measurements according to Eq. (2). Red line segments are fast-direction azimuths and delay times derived from Eq. (2) based on the model-predicted SIs obtained by integrating the sensitivity kernels (see Figure 7) with the anisotropy model in Figure 12 according to Eq. (4). Names of major faults and tectonic blocks are the same as in Figure 1.

2.3 Multiscale inversion for 3D anisotropic structure

We implement the full-wave multiscale anisotropy tomography framework developed by Lin et al.

(2014b). Here we briefly describe our methodology. Interested readers may consult Lin et al. (2014b) for a full description of the method.

Becker et al. (2006) point out that upper-mantle anisotropy is to first-order hexagonal and the hexagonal parameters ε (describing P-wave anisotropy), γ (describing S-wave anisotropy) and δ (an extra parameter describing the shape of P- and S-wave slowness surfaces) are strongly correlated. Furthermore, Zhao & Chevrot (2011) demonstrated that the sensitivity of the SI of an SKS wave is mostly sensitive to γ, and is about 10 times larger than that to the isotropic heterogeneity. This allows us to considerably simplify the modeling of upper mantle anisotropy in two aspects: (1) it is sufficient to use 1D reference model; and (2) the anisotropy can be described by only two parameters: the strength of anisotropy γ and the azimuth ϕ_f of the symmetry axis of anisotropy. We assume that the symmetry axis is horizontal since the sub-vertically propagating SKS waves are insensitive to the dip angle of the symmetry axis of anisotropy (Mondal & Long, 2019). Note that the anisotropy strength γ and azimuth ϕ_f are spatially varying, and the dependence of the SI on ϕ_f is nonlinear. As documented in Favier & Chevrot (2003), we can introduce two independent parameters, $\gamma_c = \gamma\cos(2\phi_f)$ and $\gamma_s = \gamma\sin(2\phi_f)$ to enable a linear relationship with the SI measurement

$$S = \iiint \left[K_{\gamma_c}^S(\boldsymbol{r})\gamma_c(\boldsymbol{r}) + K_{\gamma_s}^S(\boldsymbol{r})\gamma_s(\boldsymbol{r})\right]d\boldsymbol{r}, \tag{4}$$

where $K_{\gamma_c}^S$ and $K_{\gamma_s}^S$ are the Fréchet sensitivity kernels of the splitting intensity S to γ_c and γ_s, respectivity. After obtaining γ_c and γ_s from a linear inversion, we can obtain the more familiar anisotropy parameters by utilizing the relations: $\phi_f(\boldsymbol{r}) = 0.5\tan^{-1}[\gamma_s(\boldsymbol{r})/\gamma_c(\boldsymbol{r})]$ and $\gamma(\boldsymbol{r}) = \sqrt{[\gamma_c(\boldsymbol{r})]^2 + [\gamma_s(\boldsymbol{r})]^2}$. In this study, we use PREM (Dziewonski & Anderson, 1981) as the reference model and compute the sensitivity kernels using the normal mode summation algorithm developed by Zhao & Chevrot (2011). Examples of the Fréchet kernels for γ_c and γ_s are shown in

Figure 7. Chevrot (2006) first noted the similarity between the definition of the SI in Eq. (1) and that of the traveltime delay (e.g. Dahlen et al., 2000; Zhao et al., 2000), which implies that the sensitivity kernels of the SI to anisotropy parameters exhibit the distinct banana-doughnut shapes typically seen in the sensitivities of the finite-frequency traveltimes to isotropic velocities, as shown in Figure 7.

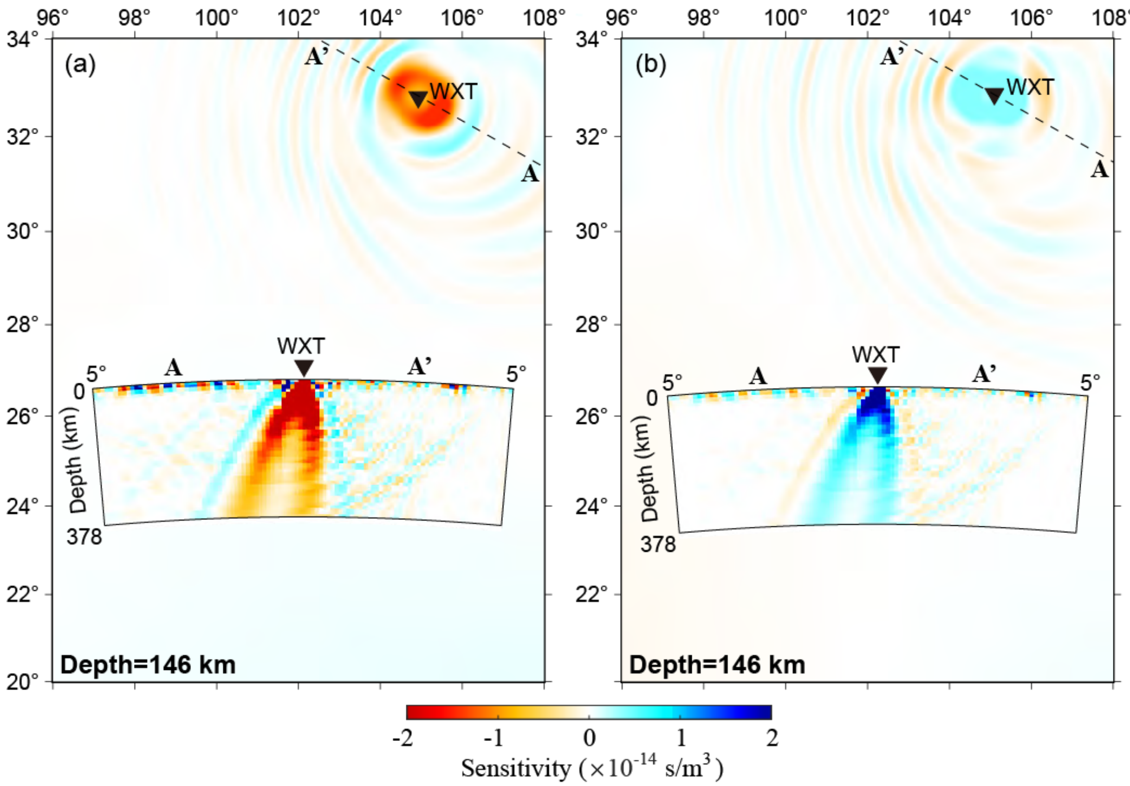

Figure 7. Examples of the sensitivity kernels of the SI to shear wave anisotropy parameters γ_c (a) and γ_s (b) shown in mapviews for the 146-km depth and in profiles (insets) along source-receiver path AA' for station WXT (blue triangle in Figure 1). The SKS wave is from the 24 June 2019 event in New Zealand with a back azimuth of 122º, and the waveforms are shown in Figure 4.

As in Lin et al. (2014b), we adopt a wavelet-based model parameterization (Chiao & Kuo, 2001) to obtain multi-scale resolutions in both sparsely- and densely-sampled regions of data coverage. The inverse problem can be expressed as:

$$(\mathbf{G}\mathbf{W}^{-1})(\mathbf{W}\mathbf{m}) = \mathbf{d}, \tag{5}$$

where **G** is Gram matrix containing the Fréchet kernels, **W** is the 3D wavelet transformation matrix,

m is the vector comprising the model parameters at spatial nodes, and $\mathbf{d}$ is the data vector of the SI measurements. In this study, we first parameterize the model by a 3D mesh with 33 × 33 nodes horizontally and 17 nodes vertically, and apply the operator $(\mathbf{W}^{-1})^T$ on each row of $\mathbf{G}$. A damped least-squares solution to the inverse problem in Eq. (5) is solved by the LSQR algorithm (Paige & Saunders, 1982), with the damping factor λ selected empirically by a series of inversion experiments (see Section 2.4), and the final model can be obtained by an inverse wavelet transform. Readers may refer to Hung et al. (2011) for implementation details of the multi-scale parameterization. The wavelet approach achieves a finer spatial resolution in regions of better data coverage and coarser resolution in less well-sampled regions, thus resolving the structure with an objective and data-driven multi-scale resolution.

2.4 Resolution tests

Careful selection of the damping factor λ and objectively evaluating the resolution for a given dataset in an inversion problem is paramount to interpreting the inversion results. Thus, it is important to characterize how reliable our anisotropic models are, and to restrict our interpretations to robust features that are well-resolved and required by the observations.

We present three sets of resolution tests to illustrate the selection of the optimal damping factor and the resulting resolution of our SI dataset. Given the input model in a resolution test, the SI is predicted for each SKS path in our final dataset by integrating the products of 3D sensitivity kernels with the distributions of γ_c and γ_s in the input model according to Eq. (4). A Gaussian noise with the same standard deviation as our final inversion dataset (0.074 s) is added to the SI predictions. We first perform a series of tests using checkerboards of two different sizes (1º x 1º and 1.5º x 1.5º) with horizontally alternating azimuthal angles of fast axes $\phi_f = 90^{\circ}$ and $\phi_f = 45^{\circ}$ but a fixed anisotropy strength $\gamma = 4\%$. Figure 8 shows the input and recovered models for different values of the damping factor λ at a depth of 55 km for the 1° x 1° checkerboard test. The effect of damping factor on the anisotropy pattern in the inversion result is obvious. The recovery results suggest an optimal damping factor of $\lambda = 4$, and the checkerboard pattern is well-resolved in most parts of the study area except in the northwest and southeast corners where stations are more sparse. Results for recovered models at different depths as well as for 1.5° x 1.5° checkerboards are presented in Figures S1 and S3 in Supporting Information.

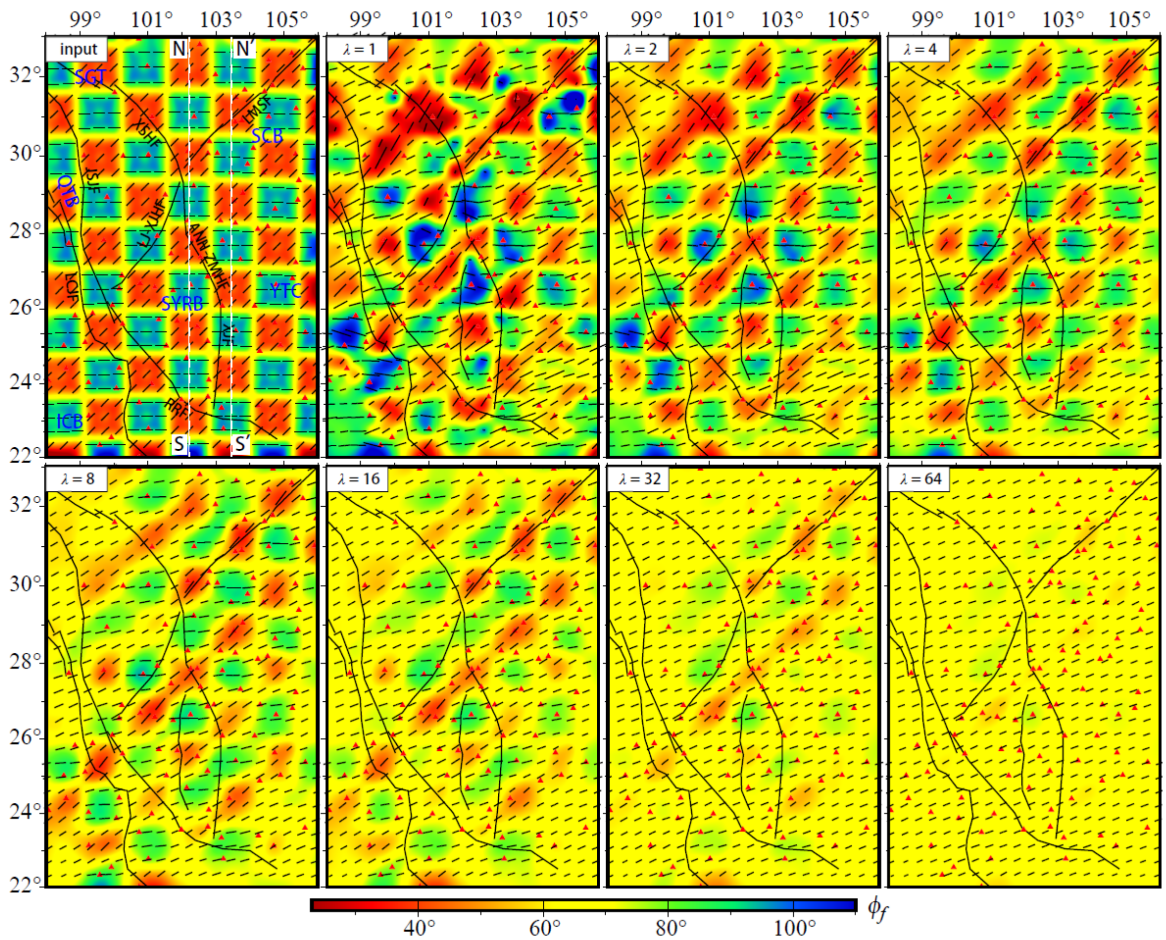

Figure 8. Resolution tests for the azimuth of symmetry axis using 1° x 1° checkerboard. (Top-left) The input model has horizontally alternating azimuthal angles of fast axes $\phi_f = 90^\circ$ and $\phi_f = 45^\circ$ shown by both the color and the directions of the line segments, and a fixed anisotropy strength $\gamma = 4\%$ represented by the lengths of the line segments. The two white dashed lines show the locations of profiles NS and N'S' in Figure 11. The other panels show the recovered models at a depth of 55 km for different damping factors λ. We choose $\lambda = 4$ as the optimal value for the

damping factor (top-right panel). Red triangles show locations of stations used.

In the second set of tests, we use input checkerboard models with a fixed azimuthal angle of symmetry axis $\phi_f = 22.5^\circ$ but alternating perturbations of anisotropy strength of $\delta\gamma = \pm 3\%$ relative to a background anisotropy strength of $\gamma = 4\%$. Figure 9 shows the recovery results at the depth of 55 km using different damping factors for the 1º x 1º input checkerboard model. Results for recovered models at different depths as well as for 1.5º x 1.5º checkerboards are presented in Figures S2 and S4 in Supporting Information.

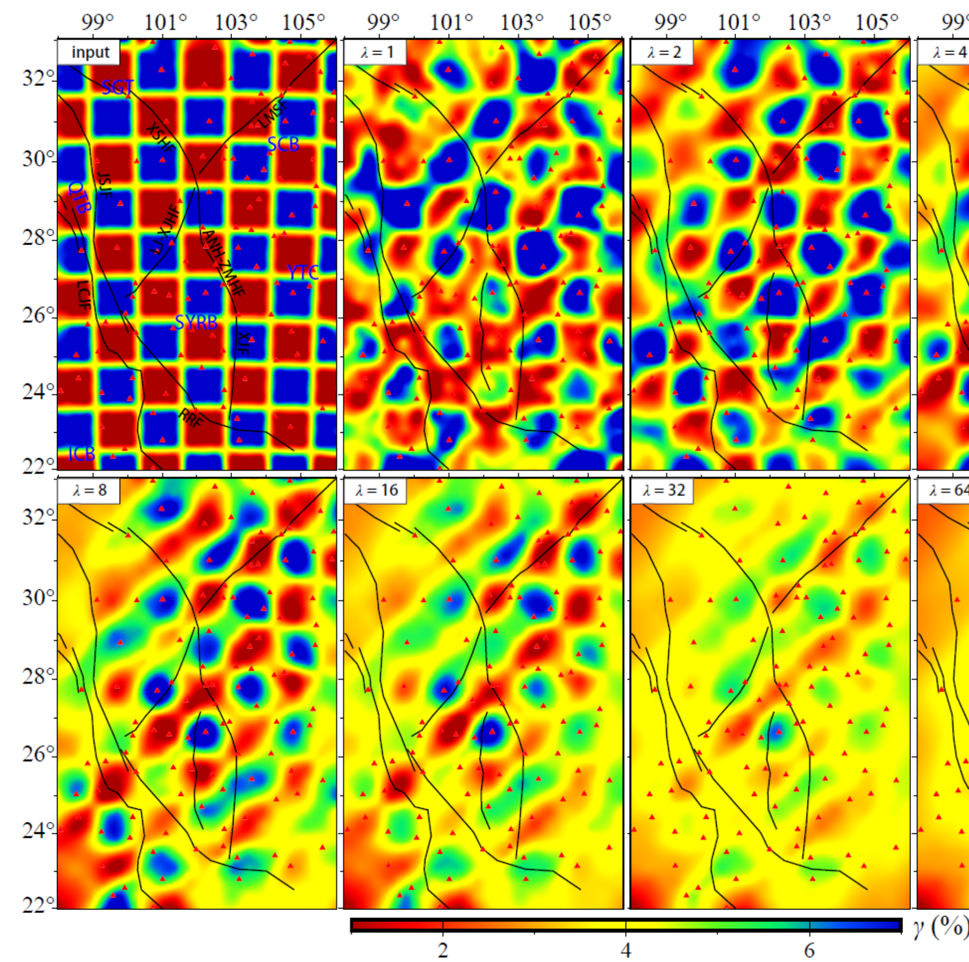

Figure 9. Resolution test using 1º x 1º checkerboard. (Top-left) The input model has horizontally alternating anisotropy strengths shown by the colors representing perturbations of $\delta\gamma = \pm 3\%$ relative to a background anisotropy strength of $\gamma = 4\%$ and a fixed azimuthal angle of symmetry axis $\phi_f = 22.5^\circ$. The other panels show the recovered models at a depth of 55 km for different

damping factors λ. We choose $\lambda = 4$ as the optimal value for the damping factor (top-right panel). Red triangles show locations of stations used.

The tests in Figures 8 and 9 both show that the damping factor of $\lambda = 4$ yields the best resolved checkerboard pattern. For convenience, resolution test results at different depths for damping factor $\lambda = 4$ are collected and displayed in Figure 10.

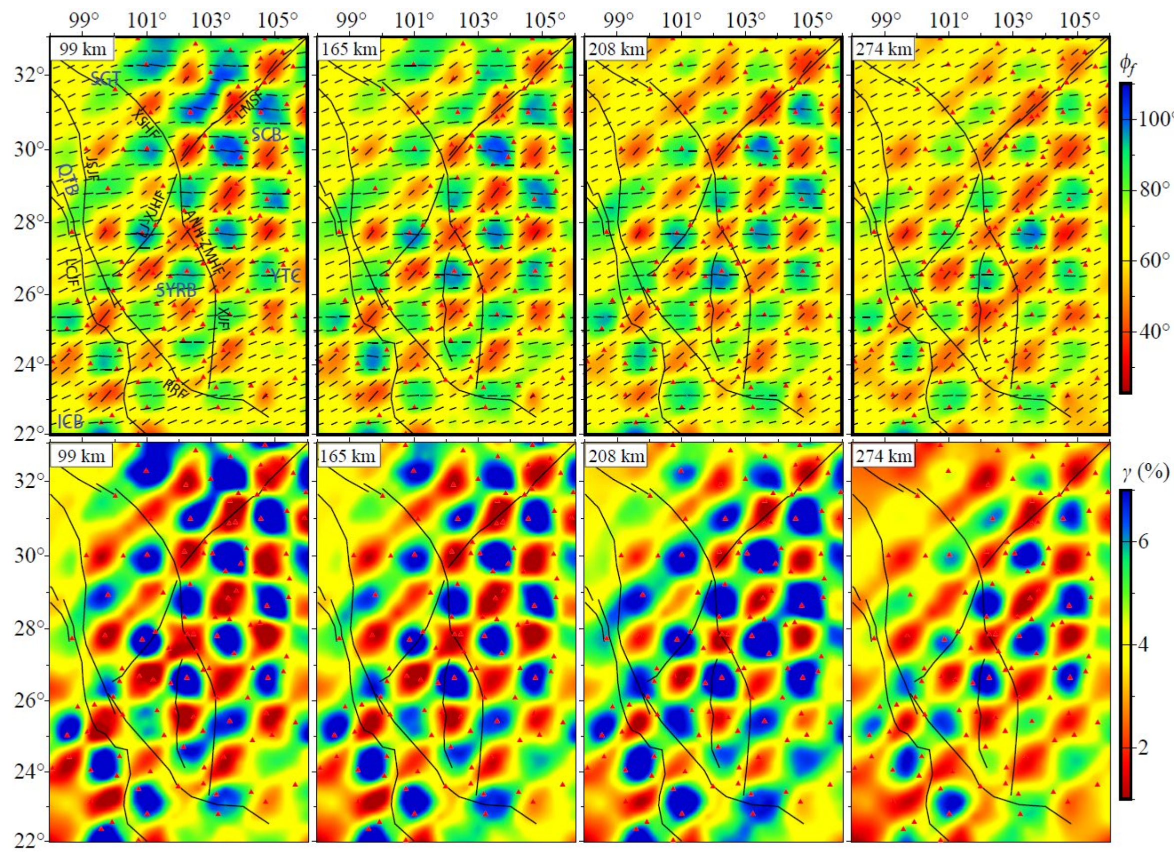

Figure 10. Resolution test using 1º x 1º checkerboard with damping factor $\lambda = 4$. (Upper panels) Recovered model at the depths of 99 km, 165 km, 208 km and 274 km for an input model having horizontally alternating azimuthal angles of fast axes $\phi_f = 90^{\circ}$ and $\phi_f = 45^{\circ}$ with a fixed anisotropy strength $\gamma = 4\%$. The input model and the recovered model at 55-km depth are shown in Figure 8. (Lower panels) Recovered model at the depths of 99 km, 165 km, 208 km and 274 km for an input model with horizontally alternating anisotropy strengths of $\gamma = 1\%$ and $\gamma = 7\%$ with a fixed azimuthal angle of symmetry axis $\phi_f = 22.5^{\circ}$. The input model and the recovered model at 55-km depth are shown in Figure 9. Red triangles show locations of stations used.

The third set of tests is intended to probe the depth resolution of our SI dataset with full-waveform anisotropy tomography. We use input models with a fixed anisotropy strength of $\gamma =$ 4% but several layers of alternating azimuthal angles of symmetry axes. Figure 11 shows the recovery results for a 4-layer input model along a north-south vertical cross-section (cross-section NS in the top-left panel of Figure 8) for different damping factors.

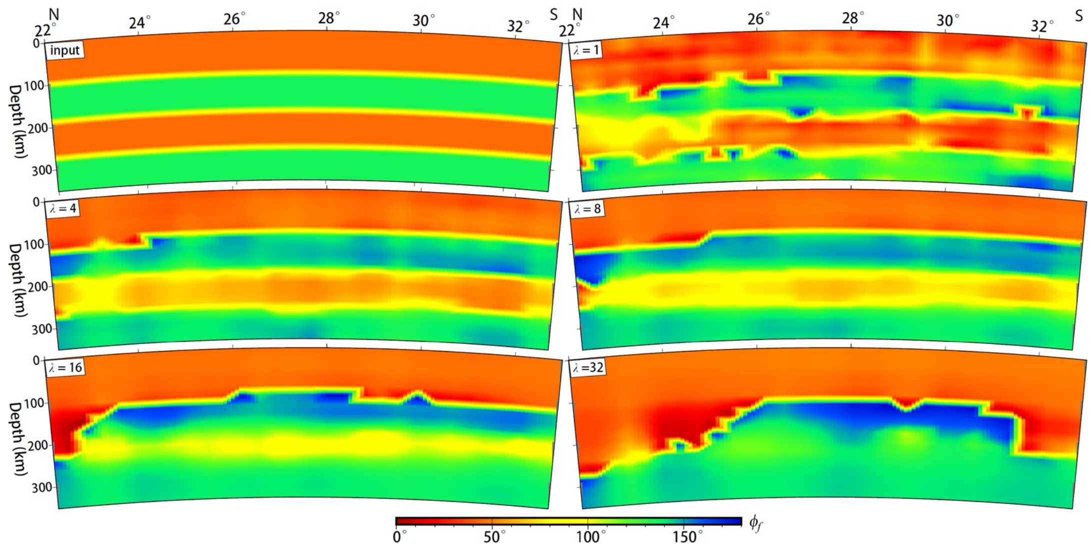

Figure 11. Resolution tests for an input model with 4 layers of alternating azimuthal angles of symmetry axes $\phi_f = 45^\circ$ and $\phi_f = 135^\circ$ but a fixed anisotropy strength of $\gamma = 4\%$. Shown here are the input model (top-left panel) and recovered models for different damping factors λ along the north-south cross-section NS through the middle of the study region (see top-left panel in Figure 8). The optimal damping is $\lambda = 4$ (middle-left panel).

Recovered models along another profile as well as for a 2-layer input model are presented in Supporting Information (Figures S5-S8). These results also suggest an optimal damping factor of $\lambda = 4$ in most parts of the study area. Based on all the resolution test results, we determine $\lambda = 4$ to be the optimal damping factor for the SI data inversions in this study.

The above resolution tests demonstrate that with the available distributions of seismic stations and teleseismic earthquakes, our SKS wave SI dataset can resolve reasonably well the shear-wave azimuthal anisotropy with a horizontal dimension of 1º x 1º and a vertical thickness of ~100 km in the main part of the study region. Near the western border and in the SE corner, the resolution is poor due to larger station spacing and fewer crossing SKS ray paths.

3 Result

As stated in Section 2.2, our final dataset contains 5,216 SI measurements at 111 permanent seismic stations from 470 events, which are used to invert for the 3D azimuthal anisotropy structure of the study region. Figure 12 displays our inverted model at five representative depths.

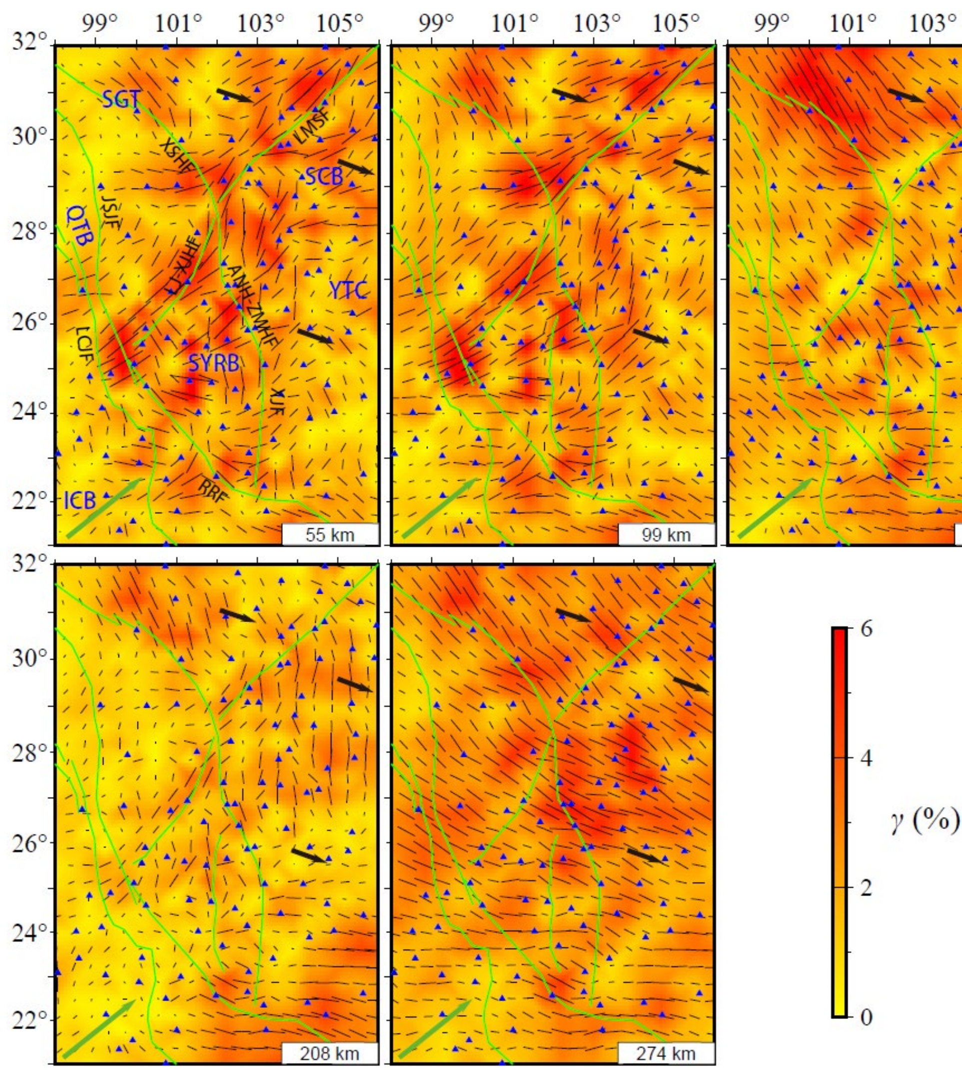

Figure 12. Three-dimensional anisotropic model for southeast margin of the Tibetan Plateau at 55 km, 99 km, 165 km, 208 km and 274 km depths. The anisotropy strength and the azimuth of the fast axes are shown by the background color and the black line segments, respectively. The lengths of the line segments are proportional to the anisotropy strength. The black and green arrows denote

the absolute plate motion (APM) of the Eurasian and Indian plates, respectively, according to the model NNR-MORVEL56 (Argus et al., 2011). Names of major faults and tectonic blocks are the same as in Figure 1. Blue triangles show locations of stations used.

As a first check of the inversion result, we calculate the model-predicted conventional SKS splitting time Δt and fast-direction azimuth θ by integrating the anisotropy model (Figure 12) with sensitivity kernels (Figure 7) according to Eq. (4) and compare with observations. The comparison in Figure 6 shows excellent agreement between the model-predicted splitting parameters with observations at all stations.

We also carry out a recovery test for our inversion result, in which we use the model in Figure 12 as the input model and calculate the synthetic SI data, then invert them using the same model discretization and damping factor as in the inversion of the real data. The comparison in Figure 13 shows that the output model strongly resembles the input model at all depths. The synthetic inversion successfully reproduces all the major features of the input model.

4 Discussion

4.1 Comparison with previous results

SKS splitting observation has been widely used to investigate the upper mantle anisotropy in the southeastern margin of the Tibetan Plateau (e.g., Lev et al., 2006; Flesch et al., 2005; Wang et al., 2008; Shi et al., 2012; Chang et al., 2015; Yang et al., 2018; Liu et al., 2020; Huang & Chevrot, 2021; Li et al., 2021), with many overlapping seismic stations and teleseismic events. Here, we compare our tomography result at common stations with those of Chang et al. (2015) and Liu et al. (2020) whose SKS splitting measurements are available at the Shear Wave Splitting Product Query website (http://ds.iris.edu/spud/swsmeasurement). In Figure 14, the SKS splitting parameters (splitting times and fast-direction azimuths) predicted by our model in Figure 12 are compared with those from the above two studies.

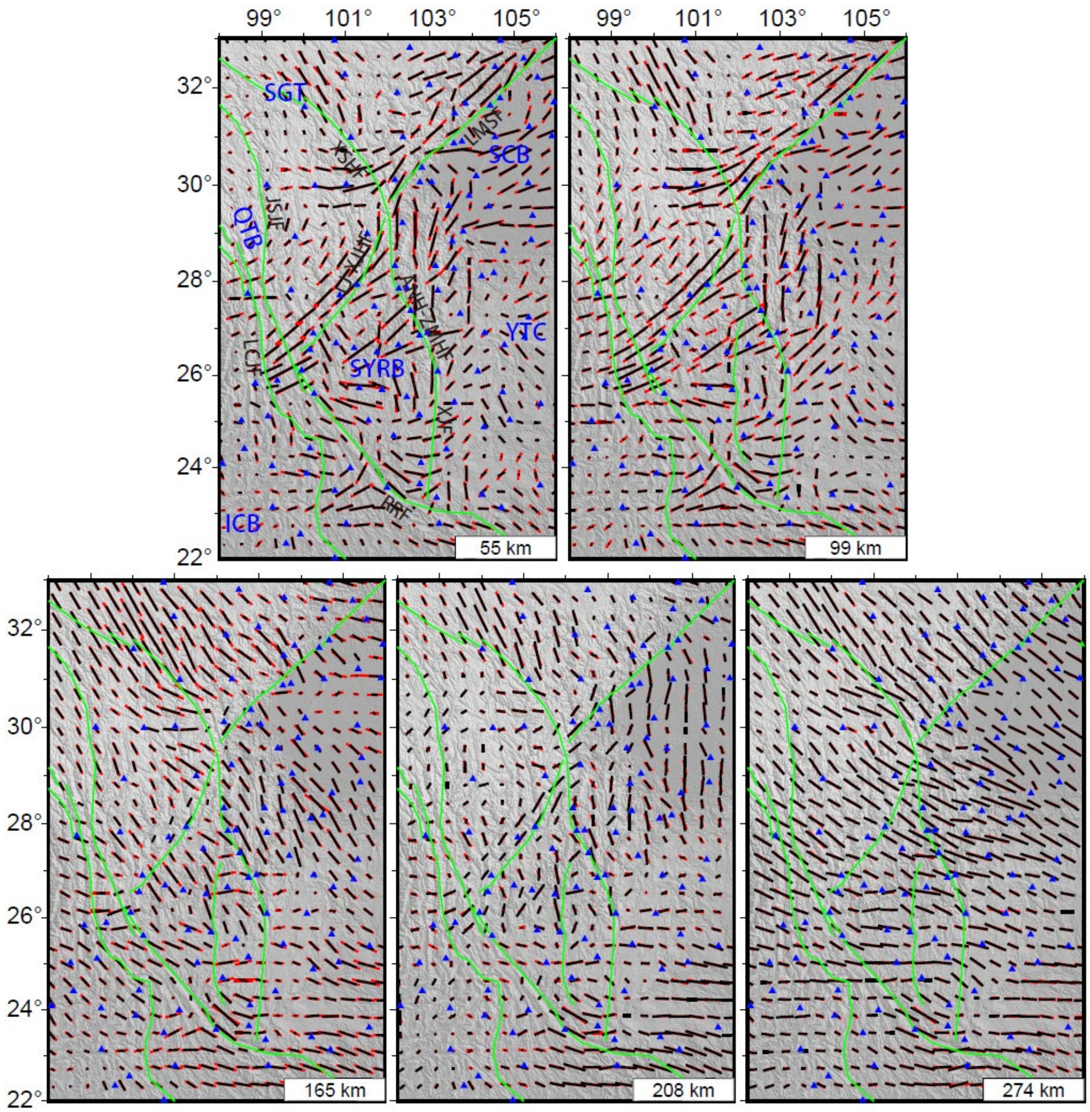

Figure 13. Result of the recovery test. The recovered and input anisotropic models are compared at five depths marked at the bottom-right corner in each panel. Black and red line segments denote the directions of fast axes in the input and recovery models, respectively, and their lengths indicates the anisotropy strength. Names of major faults and tectonic blocks are the same as in Figure 1. Blue triangles show locations of stations used.

Figure 14 shows that the fast axes determined from our tomographic results are in good agreement with previous studies at most stations. Major differences occur at two stations in the southern tip of the SCB (highlighted by the blue ellipse in Figure 14), where anomalously large splitting times can be seen in the results of Liu et al. (2020), shown by the red line segments. There are also discrepancies in both delay time and fast-axis azimuth at a few stations (highlighted by the red ellipses in Figure 14) in the SYRB where Chang et al. (2015) reported large splitting times and nearly NS fast axes, whereas our model predicts moderate-to-small splitting times and more EW orientation of fast axes. Note that a strictly quantitative comparison of different studies is difficult due to differences in earthquake and window selections, data processing and frequency bands used in the measurement of SKS splitting parameters.

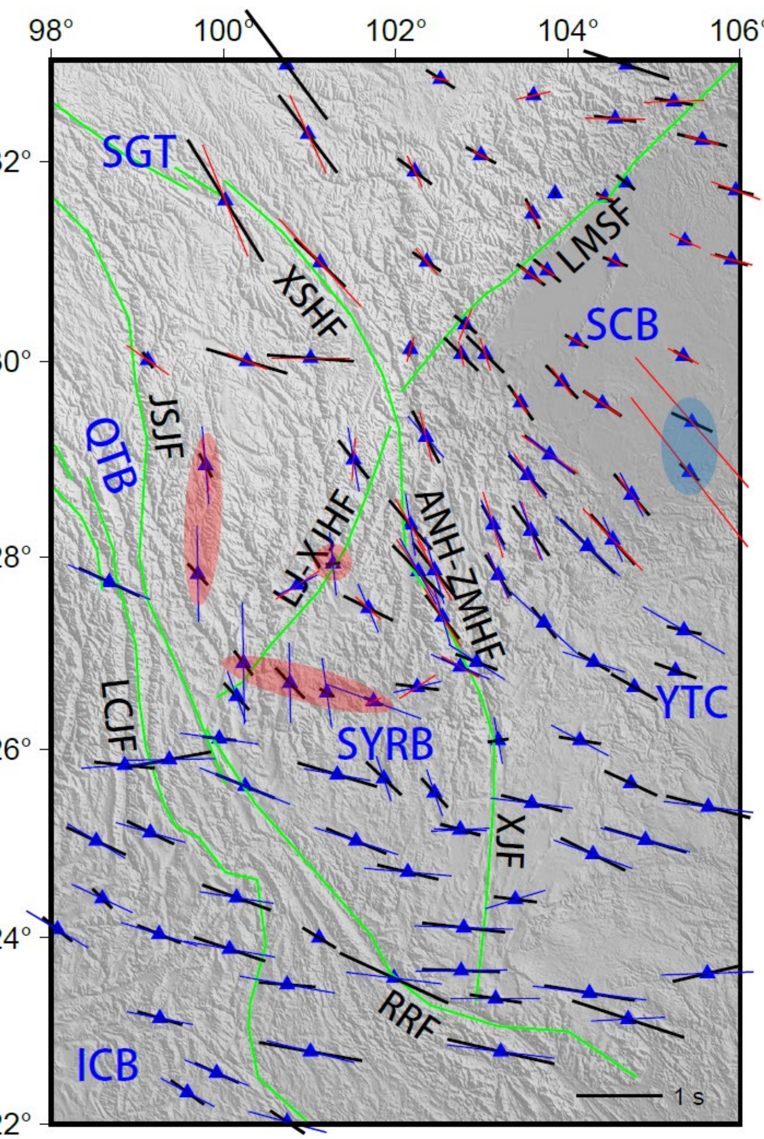

Figure 14. Comparison of SKS splitting times and fast axis directions predicted by our anisotropy model (Figure 12) with previous studies. Black line segments are results from the present study, whereas

blue and red line segments show results from Chang et al. (2015) and Liu et al. (2020), respectively. Blue and red ellipses highlight stations where there are large discrepancies in splitting parameters between this study and Liu et al. (2020) and Chang et al. (2015), respectively. Names of major faults and tectonic blocks are the same as in Figure 1.

4.2 Overall variation of shear wave anisotropy

In the shear-wave anisotropy model displayed in Figure 12, we can see that the overall anisotropy strength γ can reach 6% in the lithosphere and asthenosphere under the southeastern margin of the Tibetan Plateau. Both the strength and fast-axis directions of anisotropy show strong lateral and vertical variations. Within the lithosphere (depths of 55 km and 99 km), the anisotropy is stronger in the transition zone between the Tibetan Plateau and YTC (along the LJ-XJHF and LMSF) than other regions, whereas at greater depths in the asthenosphere (e.g. 274 km), the entire region exhibits strong anisotropy with a largely NW-SE orientation of fast axis parallel to the direction of the APM (black arrows in Figure 12), which turns to more E-W direction south of 26ºN. At intermediate depths (165 km and 208 km), the anisotropy is highly variable, both in terms of strength and the direction of symmetry axis. Therefore, in the southeastern margin of the Tibetan Plateau, our model shows an apparent decoupling in the overall deformations between the lithosphere and asthenosphere, consistent with previous studies (e.g. Flesch et al., 2005).

Previous studies have reported two major features in the SKS splitting pattern in the southeastern margin of the Tibetan Plateau: an overall NW-SE direction of the fast axis and an alignment of the fast axis in nearly EW direction south of ~26ºN latitude (e. g., Lev et al., 2006; Wang et al., 2008; Chang et al., 2015; Huang & Chevrot, 2021), as shown in Figures 6 and 14. Our model suggests that this relatively simple splitting pattern observed at the surface may be a manifestation of vertically averaged complex variation of anisotropy over lithospheric and asthenospheric depths. For instance, along the

LMSF, the fast axes in the lithospheric depth (e.g. 55 km and 99 km) are mainly oriented NE-SW with relatively high anisotropy strength, but change to NW-SE in the asthenosphere. As a result, we observe relatively small SKS splitting times (< 0.5 s) with a fast-axis direction of NW-SE at the surface. On the other hand, the moderate SKS splitting times (1 s or less) and the alignments of nearly EW orientation of symmetry axes observed at the surface are resulted from a discordant anisotropy in the lithosphere and a nearly uniform EW-oriented anisotropy in the asthenosphere.

4.3 The Songpan-Ganzi Terrane

The SGT is the central portion of the Tibetan Plateau and has been elevated by the collision between the Indian and Eurasian plates. In its eastern part the eastward expansion of the terrane has been blocked by the SCB of the YTC. In our study region, the SGT occupies an area of inverted-triangle shape in the north bounded by the JSJF in the southwest and LMSF and LJ-XJHF in the southeast (Li et al., 2021). Our model shows two distinct types of anisotropy. In the area far away from the LMSF, the anisotropy is moderate to strong (3–6%) with NW-SE oriented fast axes in both lithosphere and asthenosphere, parallel to the regional APM direction (black arrows in Figure 12) and asthenospheric flow, suggesting a vertical coupling of deformation there and in agreement with Flesch et al. (2005). The NW-SE orientation of anisotropy in the SGT is consistent with previous tomography results from Rayleigh waves (Bao et al., 2020; Legendre et al., 2015) and Pn waves (Lei et al., 2014). However, in the area near the LMSF, the fast axis of anisotropy in the lithosphere (e.g. 55 km and 99 km depths) becomes NE-SW, parallel to the proposed lithospheric material flow as a result of the resistance of the SCB to the eastward expansion of the Tibetan Plateau at LMSF. Near the LMSF, the lithospheric material of the SGT appears to come apart at ~102° longitude, going in the opposite NE and SW directions. In the asthenosphere, the fast axis of anisotropy returns to NW-SE, consistent with the regional APM direction. The relatively sharp turn of the fast axis of the lithospheric anisotropy from SE-NW to NE-SW in the southern tip of SGT is a clear evidence for the redirection of the lithospheric flow from eastward to southward in the southeastern margin of the Tibetan Plateau.

4.4 The Yangtze Craton

The YTC is a Precambrian continental block which was accreted to the North China Craton in the Triassic. Our study region covers the western margin of the YTC, namely the SCB and SYRB, and the model in Figure 12 shows that the anisotropy in the region varies significantly both horizontally and vertically, as a result of the complex geodynamic evolution of the YTC involving multiple rounds of lithospheric reactivation, such as the Permian-Triassic Emeishan flood basalt eruption (e.g. Xu et al., 2001), as well as interactions with surrounding tectonic blocks. In our anisotropy model, the SCB exhibits a moderate anisotropy with a NE-SW orientation near the LMSF at shallow depths (e.g. 55 km and 99 km), presumably the effect of dominant shearing in the vicinity of the LMSF by the moving SGT lithosphere in NE and SW directions. Further east, EW compression gradually takes over NE-SW shear at shallow depths, and the fast axis of anisotropy turns to more EW (e.g. 55 km, 99 km and 165 km). This turn of anisotropy from NE-SW to more EW away from the LMSF has also been observed in surface-wave studies (e.g. Zhang et al., 2023). At greater depth in the lithosphere (208 km in Figure 12), the anisotropy under the SCB becomes nearly NS, which is consistent with a frozen anisotropy in the lithosphere generated by the mantle flow in the Cenozoic (Li et al., 2021) without being modified by the SGT-SCB block interaction at shallower depths. At asthenospheric depth (274 km), the anisotropy is largely aligned with the regional APM.

The anisotropy under the SYRB appears to be continuous across the ANH-ZMHF and XJF, suggesting that both fault systems are crustal boundaries where the SYRB is escaping in the southeast direction. In the lithosphere (55 km and 99 km under SYRB and above 208 km depth east of ANH-ZMHF between the SCB and 26ºN), the anisotropy has a complex pattern of relatively small-scale horizontal variations of fast-axis orientation, perhaps a result of multiple phases of lithospheric reactivations that have modified the previously frozen anisotropy. In the asthenosphere (> 100 km depth in SYRB and > 200 km between the SCB and 26ºN), the anisotropy largely follows the direction of the regional APM or mantle flow. In the 208-km depth plot of the model in Figure 12, the azimuthal anisotropy south of the SCB is very weak, which may indicate a more complex local mantle flow pattern due to the regionally predominant NW-SE mantle flow being disturbed by the root of the YTC lithosphere. South of 26ºN, the anisotropy under the YTC is returns to largely parallel to the direction of APM.

4.5 Anisotropy south of 26ºN latitude

All SKS splitting studies in the southeastern margin of the Tibetan Plateau have shown the that the SKS splitting south of 26ºN latitude appears to be consistently oriented in the EW direction. Our model suggests that this apparently simple pattern is resulted predominantly from strong EW oriented azimuthal anisotropy generated by the EW asthenosphere flow due to the eastward subduction of the Indian Plate under Myanmar (e.g. Yang et al., 2022), and regional variation of lithospheric and asthenospheric contributions to anisotropy leads small but discernable differences in SKS splitting observations. For example, under the SYRB, the anisotropy in the lithosphere between 24ºN and 26ºN is relatively strong (55 km and 99 km in Figure 12) with different orientations of fast axes. The integration of lithospheric and asthenospheric anisotropy results in horizontally variable SKS splitting delay times and fast-axis directions observed at the surface, as shown by the stations in SYRB in Figures 6 and 14. In the rest of the study region south of 26ºN, the asthenospheric contribution dominates, and the surface SKS splitting parameters exhibit relatively uniform EW fast axes.

5 Conclusions

In this study, we have carried out a fullwave multiscale tomography to obtain the 3D model for the shear-wave anisotropy in the southeastern margin of the Tibetan Plateau. A total of 5,216 high-quality SKS splitting intensities are obtained from the broadband records of 470 teleseismic events at 111 permanent stations after a series of quality control measures. In conjunction with the 3D sensitivity kernels and a wavelet-based parameterization, this dataset is inverted to achieve a data-driven multi-scale resolution to anisotropy structure in the upper mantle.

The vertical variation of the anisotropy in our result indicates that the lithospheric and asthenospheric deformations are decoupled in the southeastern margin of the Tibetan Plateau. On the other hand, the anisotropy appears to be vertically consistent under the Songpan-Ganzi Terrane, suggesting a coupling of the deformations in the lithosphere and asthenosphere in the interior of the Tibetan Plateau.

The strength of anisotropy in our model is spatially variable and can reach 6%, with strongest anisotropy in the asthenosphere due to large-scale and relatively steady mantle flow, and in the lithosphere along the Longmenshan Fault and Lijiang-Xiaojinhe Fault, presumably due to large shearing effect generated by the relative movement between the Songpan-Ganzi Terrane and the Yangtze Craton.

The azimuth of the fast axis of anisotropy in the asthenosphere largely follows the direction of regional absolute plate motion or mantle flow, i.e. mostly SE beneath the Songpan-Ganzi Terrane and the Yangtze Craton and nearly east-west south of 26ºN latitude. In the lithosphere, however, the fast axis is highly variable. In the Sichuan Basin, the frozen anisotropy dominates in the deep lithosphere; whereas at shallower depths, the anisotropy is modified by the interaction with the Songpan-Ganzi Terrane into SW in the vicinity of the Longmenshan Fault and nearly EW further east. In the Sichuan-

Yunnan Rhombic Block and east of the Anninghe-Zemuhe Fault, the azimuth of the fast axis of anisotropy exhibits complex spatial pattern due to multiple phases of lithospheric reactivation. The vertical integration of the contributions from complex lithospheric anisotropy and relatively uniform asthenospheric anisotropy gives rise to the seemingly simple pattern of conventional SKS splitting parameters observed at the surface. Our 3D model of azimuthal anisotropy provides important new insights into the lithospheric and asthenospheric dynamics in the southeastern margin of the Tibetan Plateau.

Acknowledgments

This work has been supported by the National Natural Science Foundation of China (NSFC Grants U1939202, 41974046). Y.L. has been supported by the 68th China Postdoctoral Science Foundation under Grant 2020M680205.

Data Availability Statement

The processed SKS waveforms and their corresponding splitting intensities as well as the final inverted anisotropic model can be accessed at https://doi.org/10.5281/zenodo.8232748. Most of the figures are generated using the Generic Mapping Tools (Wessel et al., 2019, https://www.generic-mapping-tools.org).

References

Argus, D. F., Gordon, R. G., & DeMets, C. (2011). Geologically current motion of 56 plates relative to the no-net-rotation reference frame. *Geochemistry, Geophysics, Geosystems*, *12*(11). doi: 10.1029/2011GC003751

Bao, X., Song, X., Eaton, D. W., Xu, Y., & Chen, H. (2020). Episodic lithospheric deformation in eastern Tibet inferred from seismic anisotropy. *Geophysical Research Letters*, 47(3). doi: 10.1029/2019gl085721

Becker, T. W., Chevrot, S., Schulte-Pelkum, V., & Blackman, D. K. (2006). Statistical properties of seismic anisotropy predicted by upper mantle geodynamic models. *Journal of Geophysical Research: Solid Earth*, 111(B8). doi: 10.1029/2005JB004095

Cai, Y., Wu, J., Fang, L., Wang, W., & Yi, S. (2016). Crustal anisotropy and deformation of the southeastern margin of the Tibetan Plateau revealed by Pms splitting. *Journal of Asian Earth Sciences*, 121, 120–126. doi: 10.1016/j.jseaes.2016.02.005

Chang, L.-J., Ding, Z.-F., & Wang, C.-Y. (2015). Upper mantle anisotropy beneath the southern segment of north-south tectonic belt, China. *Chinese Journal of Geophysics (in Chinese)*, 58(11), 4052–4067. doi: 10.6038/cjg20151114

Chevrot, S. (2000). Multichannel analysis of shear wave splitting. *Journal of Geophysical Research: Solid Earth*, 105(B9), 21579–21590. doi: 10.1029/2000JB900199

Chevrot, S. (2006). Finite-frequency vectorial tomography: a new method for high-resolution imaging of upper mantle anisotropy. *Geophysical Journal International*, 165(2), 641–657. doi: 10.1111/j.1365-246X.2006.02982.x

Chiao, L. Y., & Kuo, B. Y. (2001). Multiscale seismic tomography. *Geophysical Journal International*, 145(2), 517-527. doi: 10.1046/j.0956-540x.2001.01403.x

Dahlen, F., Hung, S.-H., & Nolet, G. (2000). Fréchet kernels for finite-frequency travel- times—I. Theory. *Geophysical Journal International*, 141(1), 157-174. doi: 10.1046/j.1365-246X.2000.00070.x

Dziewonski, A. M., & Anderson, D. L. (1981). Preliminary reference Earth model, *Physics of the Earth and Planetary Interior,* 25**,** 297–356.

Favier, N., & Chevrot, S. (2003). Sensitivity kernels for shear wave splitting in transverse isotropic media. *Geophysical Journal International*, 153(1), 213–228. doi: 10.1046/j.1365-246X.2003.01894.x

Flesch, L. M., Holt, W. E., Silver, P. G., Stephenson, M., Wang, C.-Y., & Chan, W. W. (2005). Constraining the extent of crust–mantle coupling in central Asia using GPS, geologic, and shear wave splitting data. *Earth and Planetary Science Letters*, 238(1-2), 248-268. doi: 10.1016/j.epsl.2005.06.023

Han, C., Xu, M., Huang, Z., Wang, L., Xu, M., Mi, N., Yu, D., Guo, T., Wang, H., Hao, S., Tia, M., & Bi, Y. (2020). Layered crustal anisotropy and deformation in the SE Tibetan Plateau revealed by Markov- Chain-Monte-Carlo inversion of receiver functions. *Physics of the Earth and Planetary Interiors*, 306 , 106522. doi: 10.1016/j.pepi.2020.106522

Hu, J., Su, Y., Zhu, X., & Chen, Y. (2005). S-wave velocity and Poisson's ratio structure of crust in Yunnan and its implication. *Science in China Series D: Earth Sciences*, 48(2), 210–218. doi: 10.1360/03yd0062

Huang, J., Zhao, D., & Zheng, S. (2002). Lithospheric structure and its relationship to seismic and volcanic activity in southwest China. *Journal of Geophysical Research: Solid Earth*, 107(B10), ESE–13. doi: 10.1029/2000JB000137

Huang, P., Gao, Y., & Xue, B. (2022). Advances in the deep tectonics and seismic anisotropy of the Lijiang-Xiaojinhe fault zone in the Sichuan-Yunnan block, southwestern China. *Earthquake Research Advances*, 2(1), 100116. doi: 10.1016/j.eqrea.2022.100116

Huang, R., Wang, Z., Pei, S., & Wang, Y. (2009). Crustal ductile flow and its contribution to tectonic stress in Southwest China. *Tectonophysics*, 473(3-4), 476–489. doi: 10.1016/ j.tecto.2009.04.001

Huang, Z., & Chevrot, S. (2021). Mantle dynamics in the SE Tibetan Plateau revealed by teleseismic shear-wave splitting analysis. *Physics of the Earth and Planetary Interiors*, 313, 106687. doi: 10.1016/j.pepi.2021.106687

Huang, Z., Wang, L., Xu, M., & Zhao, D. (2018). P wave anisotropic tomography of the SE Tibetan Plateau: Evidence for the crustal and upper-mantle deformations. *Journal of Geophysical Research: Solid Earth*, 123(10), 8957–8978. doi: 10.1029/2018JB016048

Huang, Z., Zhao, D., & Wang, L. (2015). P wave tomography and anisotropy beneath Southeast Asia: Insight into mantle dynamics. *Journal of Geophysical Research: Solid Earth*, 120(7), 5154–5174. doi: 10.1002/2015JB012098

Hung, S. H., Chen, W. P., & Chiao, L. Y. (2011). A data-adaptive, multiscale approach of finite-frequency, traveltime tomography with special reference to P and S wave data from central

Tibet. *Journal of Geophysical Research: Solid Earth*, 116. doi: 10.1029/2010JB008190

Kind, R., Yuan, X., Saul, J., Nelson, D., Sobolev, S., Mechie, J., Zhao, W., Kosarev, G., Ni, J., Achauer, U., & Jiang, M. (2002). Seismic images of crust and upper mantle beneath Tibet: Evidence for Eurasian plate subduction. *Science*, 298(5596), 1219–1221. doi: 10.1126/science.1078115

Legendre, C. P., Deschamps, F., Zhao, L., & Chen, Q.-F. (2015). Rayleigh-wave dispersion reveals crust-mantle decoupling beneath eastern Tibet. *Scientific Reports*, 5(1), 1–7. doi: 10.1038/srep16644

Lei, J., Li, Y., Xie, F., Teng, J., Zhang, G., Sun, C., & Zha, X. (2014). Pn anisotropic tomography and dynamics under eastern Tibetan Plateau. *Journal of Geophysical Research: Solid Earth*, 119(3), 2174–2198. doi: 10.1002/2013JB010847

Lev, E., Long, M. D., & van der Hilst, R. D. (2006). Seismic anisotropy in Eastern Tibet from shear wave splitting reveals changes in lithospheric deformation. *Earth and Planetary Science Letters*, 251(3-4), 293-304. doi: 10.1016/j.epsl.2006.09.018

Li, H., Su, W., Wang, C.-Y., & Huang, Z. (2009). Ambient noise Rayleigh wave tomography in western Sichuan and eastern Tibet. *Earth and Planetary Science Letters*, 282(1-4), 201–211. doi: 10.1016/j.epsl.2009.03.021

Li, W., Chen, Y., Liang, X., & Xu, Y.-G. (2021). Lateral seismic anisotropy variations record interaction between Tibetan mantle flow and plume-strengthened Yangtze Craton. *Journal of Geophysical Research: Solid Earth*, 126, e2020JB020841. https://doi.org/10.1029/2020JB020841

Lin, Y.-P., Zhao, L., & Hung, S.-H. (2014a). Full-wave effects on shear wave splitting, *Geophysical Research Letters*, 41(3), 799–804. doi: 10.1002/2013GL058742

Lin, Y.-P., Zhao, L., & Hung, S.-H. (2014b). Full-wave multiscale anisotropy tomography in Southern California. *Geophysical Research Letters*, 41(24), 8809–8817. doi: 10.1002/2014GL061855

Link, F., Reiss, M. C., & Rümpker, G. (2022). An automatized XKS-splitting procedure for large data sets: Extension package for SplitRacer and application to the USArray. *Computers & Geosciences*, 158, 104961. doi: 10.1016/j.cageo.2021.104961

Liu, J., Wu, J., Wang, W., Fang, L., & Chang, K. (2020). Seismic anisotropy beneath the eastern margin of the Tibetan Plateau from SKS splitting observations. *Tectonophysics*, 785, 228430.

doi: 10.1016/j.tecto.2020.228430

Liu, Q. Y., van Der Hilst, R. D., Li, Y., Yao, H. J., Chen, J. H., Guo, B., Qi, S. H., Wang, J., Huang, H., & Li, S. C. (2014). Eastward expansion of the Tibetan Plateau by crustal flow and strain partitioning across faults. *Nature Geoscience*, 7(5), 361–365. doi: 10.1038/NGEO2130

Long, M. D., & Becker, T. W. (2010). Mantle dynamics and seismic anisotropy. *Earth and Planetary Science Letters,* 297(3-4), 341–354.

Mondal, P., & Long, M. D. (2019). A model space search approach to finite-frequency SKS splitting intensity tomography in a reduced parameter space. *Geophysical Journal International*, 217, 238-256. doi: 10.1093/gji/ggz016

Mondal, P., & Long, M. D. (2020). Strong seismic anisotropy in the deep upper mantle beneath the Cascadia backarc: Constraints from probabilistic finite-frequency SKS splitting intensity tomography. *Earth and Planetary Science Letters*, 539, 116172. doi: 10.1016/j.epsl.2020.116172

Monteiller, V., & Chevrot, S. (2011). High-resolution imaging of the deep anisotropic structure of the San Andreas Fault system beneath southern California. *Geophysical Journal International*, 186(2), 418-446. doi: 10.1111/j.1365-246X.2011.05082.x

Paige, C. C., & Saunders, M. A. (1982). LSQR–an algorithm for sparse linear-equations and sparse least-squares. *ACM Transactions on Mathematical Software*, 8(1), 43–71.

Pasyanos, M. E., Masters, T. G., Laske, G., & Ma, Z. (2014). LITHO1. 0: An updated crust and lithospheric model of the Earth. *Journal of Geophysical Research: Solid Earth*, 119(3), 2153–2173. doi: 10.1002/2013JB010626

Quatieri, T. F. (2006). *Discrete-time Speech Signal Processing: Principles and Practice*. Pearson Education India.

Royden, L. H., Burchfiel, B. C., & van der Hilst, R. D. (2008). The geological evolution of the Tibetan Plateau. *Science*, 321(5892), 1054–1058. doi: 10.1126/science.1155371

Shen, Z.-K., Lü, J., Wang, M., & Bürgmann, R. (2005). Contemporary crustal deformation around the southeast borderland of the Tibetan Plateau. *Journal of Geophysical Research: Solid Earth*, 110(B11). doi: 10.1029/2004JB003421

Shi, Y., Gao, Y., Su, Y., & Wang, Q. (2012). Shear-wave splitting beneath Yunnan area of Southwest China. *Earthquake Science*, 25(1), 25–34. doi: 10.1007/s11589-012-0828-4

Sieminski, A., Paulssen, H., Trampert, J., & Tromp, J. (2008). Finite-frequency SKS splitting:

measurement and sensitivity kernels. *Bulletin of the Seismological Society of America*, 98(4), 1797–1810. doi: 10.1785/0120070297

Sun, Y., Niu, F., Liu, H., Chen, Y., & Liu, J. (2012). Crustal structure and deformation of the SE Tibetan plateau revealed by receiver function data. *Earth and Planetary Science Letters*, 349, 186-197. doi: 10.1016/j.epsl.2012.07.007

Wang, C.-Y., Chan, W. W., & Mooney, W. D. (2003). Three-dimensional velocity structure of crust and upper mantle in southwestern China and its tectonic implications. *Journal of Geophysical Research: Solid Earth*, *108*(B9). doi: 10.1029/2002JB001973

Wang, C.-Y., Flesch, L. M., Silver, P. G., Chang, L.-J., & Chan, W. W. (2008). Evidence for mechanically coupled lithosphere in central Asia and resulting implications. *Geology*, 36(5), 363–366. doi: 10.1130/G24450A.1

Wang, C.-Y., Lou, H., Silver, P. G., Zhu, L., & Chang, L. (2010). Crustal structure variation along 30°N in the eastern Tibetan Plateau and its tectonic implications. *Earth and Planetary Science Letters*, 289(3-4), 367–376. doi: 10.1016/j.epsl.2009.11.026

Wang, M., & Shen, Z.-K. (2020). Present-day crustal deformation of continental China derived from GPS and its tectonic implications. *Journal of Geophysical Research: Solid Earth*, 125(2), e2019JB018774. doi: 10.1029/2019JB018774

Wang, W., Wu, J., Fang, L., Lai, G., & Cai, Y. (2017). Crustal thickness and Poisson's ratio in southwest China based on data from dense seismic arrays. *Journal of Geophysical Research: Solid Earth*, 122(9), 7219–7235. doi: 10.1002/2017JB013978

Wei, W., Xu, J., Zhao, D., & Shi, Y. (2012). East Asia mantle tomography: New insight into plate subduction and intraplate volcanism. *Journal of Asian Earth Sciences*, 60, 88–103. doi: 10.1016/j.jseaes.2012.08.001

Wei, Z., & Zhao, L. (2019). Lg-Q model and its implication on high-frequency ground motion for earthquakes in the Sichuan and Yunnan region. *Earth and Planetary Physics*, 3(6), 526–536. doi: 10.26464/epp2019054

Wei, Z., & Zhao, L. (2022). P-wave velocity structure of the lower crust and uppermost mantle beneath the Sichuan-Yunnan (China) region. *Seismological Research Letters*, 93(4). doi: 10.1785/0220210357

Wessel, P., Luis, J., Uieda, L., Scharroo, R., Wobbe, F., Smith, W. H., & Tian, D. (2019). The generic mapping tools version 6. *Geochemistry, Geophysics, Geosystems*, 20(11), 5556–5564.

doi: 10.1029/2019GC008515

Xu, L., Rondenay, S., & van der Hilst, R. D. (2007). Structure of the crust beneath the southeastern Tibetan Plateau from teleseismic receiver functions. *Physics of the Earth and Planetary Interiors*, 165(3-4), 176–193. doi: 10.1016/j.pepi.2007.09.002

Xu, M., Huang, Z., Wang, L., Xu, M., Zhang, Y., Mi, N., Yu, D., & Yuan, X. (2020). Sharp lateral Moho variations across the SE Tibetan margin and their implications for plateau growth. *Journal of Geophysical Research: Solid Earth*, 125(5), e2019JB018117. doi: 10.1029/2019JB018117

Xu, Y., Chung, S.-L., Jahn, B.-m., & Wu, G. (2001). Petrologic and geochemical constraints on the petrogenesis of Permian–Triassic Emeishan flood basalts in southwestern China. *Lithos*, 58, 145–168.

Yang, S., Liang, X., Jiang, M., Chen, L., He, Y., Mon, C. T., Hou, G., Thant, M., Sein, K., & Wan, B. (2022). Slab remnants beneath the Myanmar terrane evidencing double subduction of the Neo-Tethyan Ocean. *Science Advances*, 8(34), eabo1027. doi: 10.1126/sciadv.abo1027

Yang, Y., Liang, C., Fang, L., Su, J., & Hua, Q. (2018). A comprehensive analysis on the stress field and seismic anisotropy in eastern Tibet. *Tectonics*, 37(6), 1648–1657. doi: 10.1029/2018TC005011

Yang, Y., Yao, H., Wu, H., Zhang, P., & Wang, M. (2019). A new crustal shear-velocity model in Southwest China from joint seismological inversion and its implications for regional crustal dynamics. *Geophysical Journal International*, 220, 1379–1393. https://doi.org/10.1093/gji/ggz514

Yang, Y., Zheng, Y., Chen, J., Zhou, S., Celyan, S., Sandvol, E., Tilmann, F., Priestley, K., Hearn, T. M., Ni, J. F., Brown, L. D., & Ritzwoller, M. H. (2010). Rayleigh wave phase velocity maps of Tibet and the surrounding regions from ambient seismic noise tomography. *Geochemistry, Geophysics, Geosystems*, 11(8). doi:10.1029/2010GC003119

Yao, H. J., van der Hilst, R. D., & Montagner, J. P. (2010). Heterogeneity and anisotropy of the lithosphere of SE Tibet from surface wave array tomography. *Journal of Geophysical Research: Solid Earth*, 115. doi: 10.1029/2009JB007142

Yin, A., & Harrison, T. M. (2000). Geologic evolution of the Himalayan-Tibetan orogen. *Annual Review of Earth and Planetary Sciences*, 28(1), 211–280.

Zhang, F., Wu, Q., Li, Y., Zhang, R., Sun, L., Pan, J., & Ding, Z. (2018). Seismic tomography of eastern Tibet: Implications for the Tibetan Plateau growth. *Tectonics*, 37(9), 2833–2847. doi: 10.1029/2018TC004977

Zhang, G. W., Guo, A. L., Wang, Y. J., Li, S. Z., Dong, Y. P., Liu, S. F., He, D. F., Cheng, S. Y., Lu, R. K., & Yao, A. P. (2013). Tectonics of South China Continent and its implications. *Science China Earth Sciences*, 56, 1804–1828. doi: 10.1007/s11430-013-4679-1

Zhang, P., Deng, Q., Zhang, G., Ma, J., Gan, W., Min, W., Mao, F., & Wang, Q. (2003). Active tectonic blocks and strong earthquakes in the continent of China. *Science China Earth Sciences*, 46(2), 13–24. doi: 10.1360/03dz0002

Zhang, P.-Z. (2013). A review on active tectonics and deep crustal processes of the western Sichuan region, eastern margin of the Tibetan Plateau. *Tectonophysics*, 584, 7–22. doi: 10.1016/j.tecto.2012.02.021

Zhang, Z., Wang, Y., Chen, Y., Houseman, G. A., Tian, X., Wang, E., & Teng, J. (2009). Crustal structure across Longmenshan fault belt from passive source seismic profiling. *Geophysical Research Letters*, 36(17). doi: 10.1029/2009GL039580

Zhang, Z., Yao, H., & Yang, Y. (2020). Shear wave velocity structure of the crust and upper mantle in Southeastern Tibet and its geodynamic implications. *Science China Earth Sciences*, 63, 1278–1293. https://doi.org/10.1007/s11430-020-9625-3

Zhang, Z., Feng, J., & Yao, H. (2023). 3-D azimuthal anisotropy structure reveals different deformation modes of the crust and upper mantle in the southeastern Tibetan Plateau. *Frontiers in Earth Science*, 11, 1095609. doi: 10.3389/feart.2023.1095609

Zhao, G., Unsworth, M. J., Zhan, Y., Wang, L., Chen, X., Jones, A. G., Tang, J., Xiao, Q., Wang, J., Cai, J., Li, T., Wang, Y., & Zhang, J. (2012). Crustal structure and rheology of the Longmenshan and Wenchuan Mw 7.9 earthquake epicentral area from magnetotelluric data. *Geology*, 40(12), 1139–1142. doi: 10.1130/ G33703.1

Zhao, L., & Chevrot, S. (2011). An efficient and flexible approach to the calculation of three-dimensional full-wave fréchet kernels for seismic tomography—II. Numerical results. *Geophysical Journal International*, 185(2), 939–954. doi: 10.1111/j.1365-246X.2011.04984.x

Zhao, L., Jordan, T. H., & Chapman, C. H. (2000). Three-dimensional Fréchet differential kernels for seismic delay times, *Geophysical Journal International*, 141(3), 558–576. doi: 10.1046/j.1365-246x.2000.00085.x

Zhao, L. F., Xie, X. B., He, J. K., Tian, X., & Yao, Z. X. (2013). Crustal flow pattern beneath the Tibetan Plateau constrained by regional Lg-wave Q tomography. *Earth and Planetary Science Letters*, 383, 113–122. doi: 10.1016/j.epsl.2013.09.038.